minerals

MDPI

Article

Remote Sensing, Mineralogy, and Radioactive Prospecting of the Bostonite Dykes: Radiological Hazard Evaluation

Gehad M. Saleh [1], Tamader Alhazani [2], Samir Z. Kamh [3], Basma A. El-Badry [2], Mabrouk Sami [4,5], Ioan V. Sanislav [6,*] and El Saeed R. Lasheen [7,*]

1 Nuclear Materials Authority, El-Maadi, Cairo P.O. Box 530, Egypt
2 Physics Department, Faculty of Science, Imam Mohammad Ibn Saud Islamic University (IMSIU), Riyadh 11564, Saudi Arabia
3 Geology Department, Faulty of Science, Tanta University, Tanta 31527, Egypt
4 Geosciences Department, College of Science, United Arab Emirates University, Al Ain 15551, United Arab Emirates
5 Geology Department, Faculty of Science, Minia University, El-Minia 61519, Egypt
6 Economic Geology Research Centre (EGRU), College of Science and Engineering, James Cook University, Townsville, QLD 4811, Australia
7 Geology Department, Faculty of Science, Al-Azhar University, Cairo 11884, Egypt
* Correspondence: ioan.sanislav@jcu.edu.au (I.V.S.); elsaeedlasheen@azhar.edu.eg (E.S.R.L.)

Abstract

This study investigates the dyke swarms of the Um Dwiela area in the southern Egyptian Shield through a combined approach of remote sensing, field investigations and laboratory analyses, including mineralization and radioactive prospecting. Radioelements laboratory measurements and optical remote sensing datasets are combined to detect the bostonite rocks and their radioactive mineralization. The processing of Landsat-8, Sentinel-2 and ASTER data effectively delineated the country rocks, bostonite dykes and structural elements. Field observations indicate that the dykes trend NE-SW, extending approximately 12 km with widths ranging from 1 to 13 m. These dykes have experienced multiple alteration phases, pointing to the influence of hydrothermal fluids. Uranium mineralization is structurally controlled, occurring within fractures at the contact between bostonite and metasedimentary rocks. Average measurements obtained using a NaI(Tl) analyzer reveal elevated and variable radionuclide concentrations [^{232}Th (442.25 Bq/kg), ^{238}U (608.43 Bq/kg), and ^{40}K (1141.41 Bq/kg)], all exceeding internationally permissible safety limits. Multiple radiological hazard indices further indicate a substantial radiation risk, with all values classified as high according to global standards. Consequently, the associated gamma radiation exposure poses an elevated radiological hazard concern.

Keywords: Um Dwiela Dykes; alteration zones; radioactivity; radiation health

Check for updates

Academic Editors: Fernando P. Carvalho and Emmanuel K. Atibu

Received: 2 May 2026
Revised: 27 May 2026
Accepted: 8 June 2026
Published: 10 June 2026

Copyright: © 2026 by the authors. Licensee MDPI, Basel, Switzerland. This article is an open access article distributed under the terms and conditions of the Creative Commons Attribution (CC BY) license.

1. Introduction

The radioactivity study forms a critical link between geological processes and public health, providing key insights into Earth's systems, and their direct implications for human and environmental well-being. In recent decades, this connection has driven growing scientific interest in mapping natural radiation levels to establish baseline exposure rates for populations [1–5]. Natural radionuclides concentrate mainly in granitic/phosphate rocks that represent the primary sources of terrestrial radiation [6–8].

While levels of cosmic type are subject to temporal fluctuations, terrestrial radiation is primarily controlled by localized factors including topography and soil composition [7,8].

As a result, the concentration of radioelements in rocks serves as a critical factor in determining public exposure to ionizing radiation. Natural sources account for approximately 96% of total human radiation exposure, with artificial sources contributing only 4% [1]. The presence of radionuclides in soil poses a radiological health risk when their activity concentrations exceed established safety thresholds. Elevated exposure to these radioactive elements has been linked to an increased incidence of leukemia, as well as cancers of the kidney, prostate, and skin [1,9]. Furthermore, radionuclides can enter the food chain through plant uptake from contaminated soils. Plants absorb these radioactive elements, which are subsequently transferred to humans through consumption, facilitating their accumulation in biological systems. Once ingested, natural radionuclides tend to concentrate in specific organs, posing significant risks to the digestive and endocrine systems. For instance, uranium accumulation has been documented in the kidneys, lungs, and thyroid gland, while potassium tends to accumulate in muscle tissue [10].

Optical remote sensing data with moderate scale and a good scheme of image processing techniques became sufficient to detect small-rock masses and their intruded dykes. The distinctive spectral signatures of different rock units and their associated mineralization is the base of accurate geologic and mineralogical mapping. Fortunately, the wavelengths of visible-near-infrared (VNIR) and the shortwave infrared (SWIR) regions of the multispectral sensors are able to detect different rock types with poly-mineralized zones (e.g., dykes). The results can be reliable and accurate if you take into consideration the fault/fracture systems and/or hydrothermal alteration minerals [2]. The present study is an attempt to test the capabilities of remote sensing data in detecting the bostonite swarms and their radioactive mineralization in Wadi Um Dwiela area, southeastern Desert of Egypt. The results of the remote sensing studies are integrated with fieldwork and petrographical and geochemical investigations to locate radioactive mineralization zones and their geological controls.

While previous radiological studies in the Egyptian Shield of have focused on magmatic and sedimentary rocks sequences, the dyke swarms have received limited attention despite their known association with hydrothermal uranium mineralization. This study distinguishes itself from previous work by (1) providing the comprehensive radiological characterization of bostonite dykes in the Um Dwiela area, (2) integrating remote sensing, field, petrography, ESEM-EDS mineralogy, and gamma-ray spectrometry within a single work, (3) quantifying the radiological hazard indices, (4) establishing spatial correlations between radionuclide distribution and hydrothermal alteration intensity, and (5) identifying the full radioactive mineral assemblage that governs radionuclide mobility in this setting.

2. Study Area and Geology Setting

The Egyptian crystalline rocks (Figure 1a), located in the northern Arabian-Nubian Shield, include a variety of lithology such as ophiolites, arc-related rocks, and granites [11,12] (Figure 1b). Beyond their geological significance, these rocks have economic value. They are largely untouched by ore mining and are suitable for construction and ornamentation due to their strength and appearance [13]. Moreover, the late granitic phases are notably enriched in critical metals like Nb, W, Th, Sn, Au, U, Cu, and Ta. The Um Dwiela area is situated in the southern Eastern Desert of Egypt, between latitudes 22°15′ and 22°20′ N and longitudes 33°27′ and 33°29′ E (Figure 2). The area is dissected by a prominent bostonite dyke that trends NE-SW, extending for approximately 12 km with widths ranging from 1 to 13 m. This dyke cut three distinct country rock units: metasediments and metavolcanics (Figure 3).

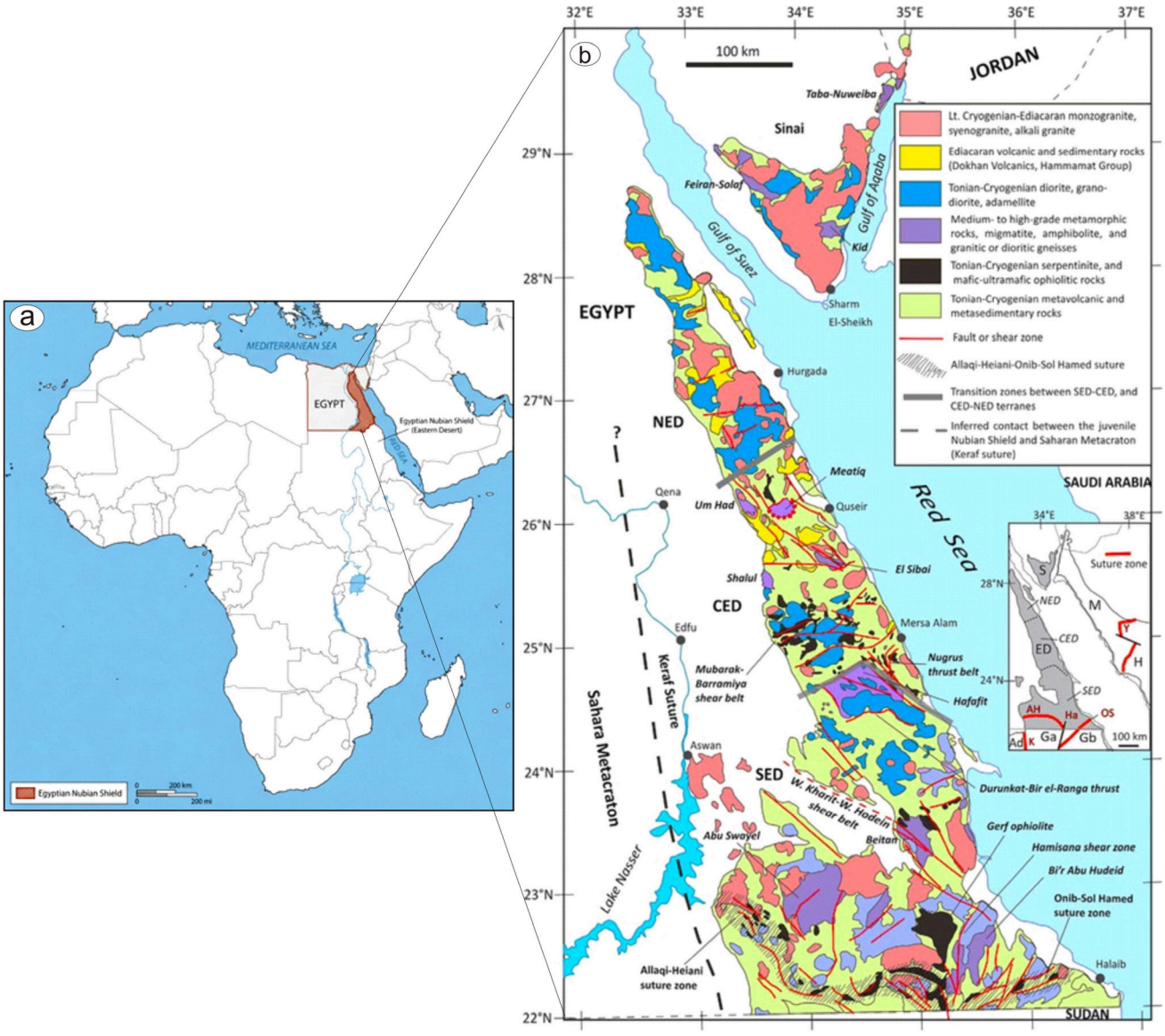

Figure 1. (**a**) Location map of the Egyptian Nubian Shied in North Africa and (**b**) basement rocks abundance [14].

Structurally, the area is dominated by two semi-perpendicular fracture trends oriented NE-SW and NW-SE. These primary trends are associated with two minor sets: NNW-SSE to N-S and ENE-WSW to E-W. The NE-SW trend represents the main structural conduit for the bostonite emplacement, which occurred during an extensional deformation phase. While these fracture systems pervasively cut the basement country rocks, they are absent in the overlying Nubian sandstones, indicating a pre-Nubian age for the deformation. The bostonite is characterized by a distinct reddish-brown coloration (Figure 3a,b), attributed to a high concentration of iron oxides. Evidence of extensive hydrothermal activity is manifested through pervasive silicification, ferrugination, fluoritization, and kaolinization.

Sampling locations covered both highly altered and weakly altered sectors to evaluate spatial variability in radionuclide distribution. Uranium mineralization is structurally controlled within this system, occurring as fracture infills, most notably at the contact zone between the bostonite dyke and the metasedimentary country rock [15]. Petrographically, the Um Dwiela bostonite consists primarily of plagioclase, occurring as prismatic crystals of dusty andesine laths, along with minor orthoclase, quartz, and amphibole. These constituents are embedded within a fine cryptocrystalline groundmass that exhibits trachytic

and flow textures. Accessory minerals include zircon, observed as well-developed crystals enclosed within plagioclase; uranium minerals, notably kasolite, which appears as subhedral crystals restricted to plagioclase; and iron oxides, widely disseminated throughout the section (Figure 3c–f).

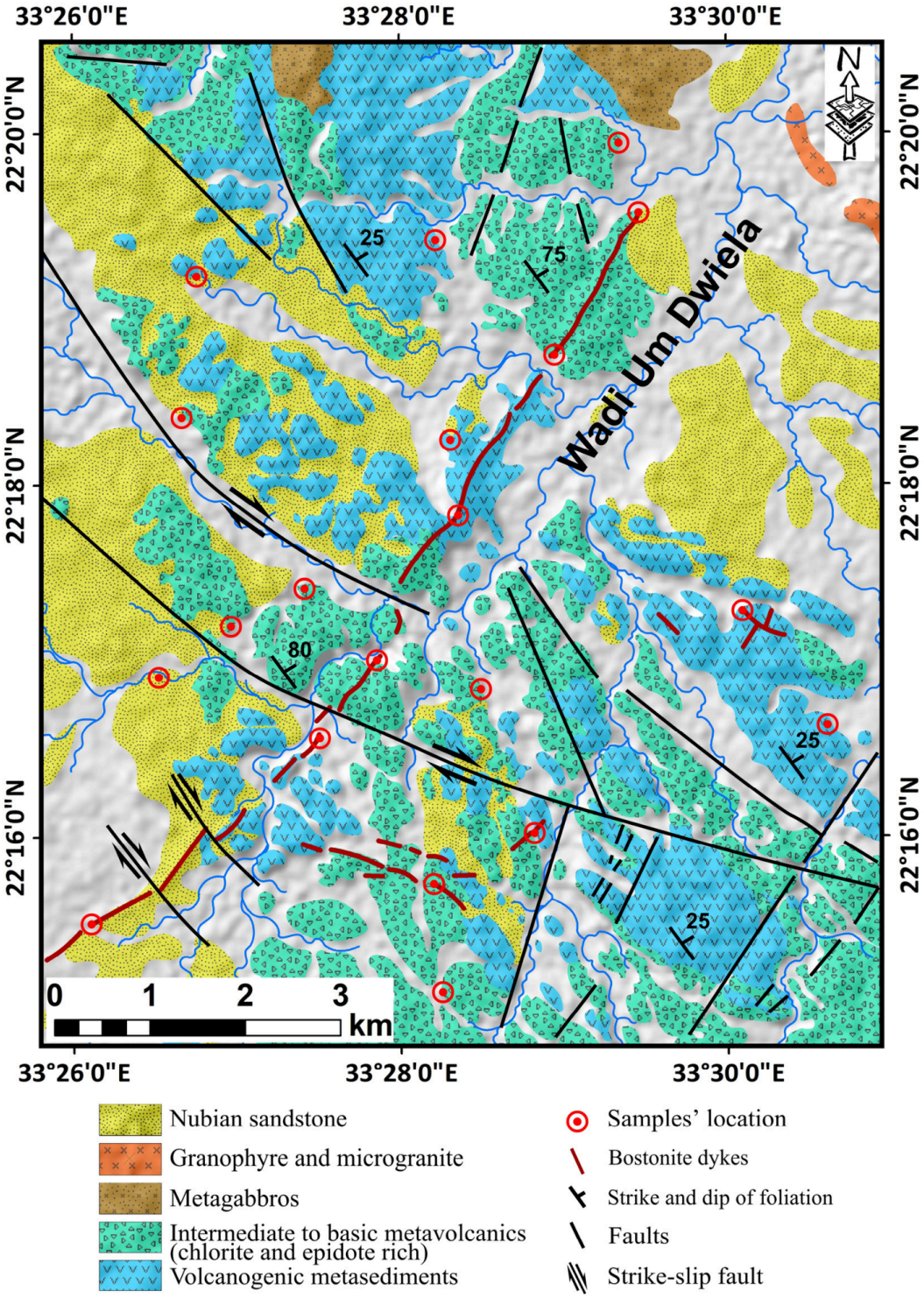

Figure 2. Um Dwiela geologic map, southern Eastern Desert, Egypt modified after [15].

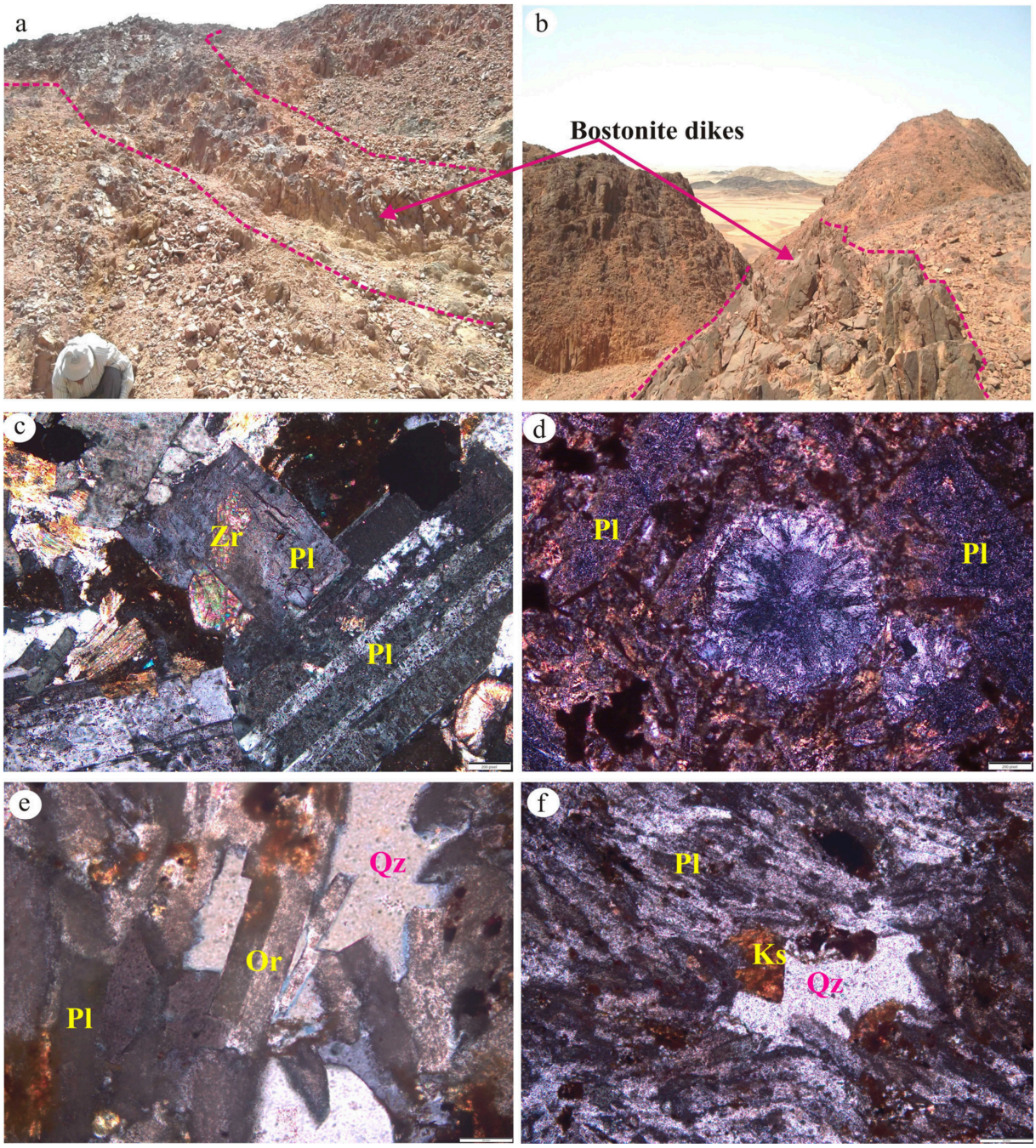

Figure 3. (**a**,**b**) Field of Um Dwiela bostonite photographs cutting metasediment and metavolcanics, respectively. Photomicrographs reveal (**c**) dusty plagioclase (Pl) enclosing zircon (Zr) crystals; (**d**) spheriolitic texture mantled by amphibole; (**e**) kaolinitized orthoclase (Or); and (**f**) subhedral kasolite (Ks) restricted in plagioclase and quartz (Qz).

3. Material and Utilized Technique Characterization

3.1. Remote Sensing Data

Three optical remote sensing datasets are used in the present study to differentiate the country rock units and altered minerals bearing radio elements. They are Landsat-8 OLI/TIRS (L2), Sentinels 2A (L2A) and ASTER (LB). The spatial resolution up to 10 m and the wide spectral range of these images including visible, NIR, and SWIR are sufficient to detect the bostonite dykes and their radioactive minerals abundance. These datasets were processed by preprocessing procedures to be appropriate to distinguish the different rock units, to detect the bostonite dykes and their radioactive contents as well as to extract

structural elements. The three images are cloud-free and they are geometrically corrected to the Universal Transversal Mercator (UTM; zone 36) and datum of WGS84. Radiometric correction was applied using the ENVI 5.3 function to transform the digital numbers (DN) to surface reflectance values. The Landsat-8 and Sentinel-2A images were atmospherically corrected using Fast Line-of-Sight Atmospheric Analysis of Spectral Hypercubes (FLAASH), whereas ASTER images were corrected using the Internal Average Relative Reflection (IARR). This technique is a common calibration technique for mineralogical mapping in arid regions. Layer-stacking, mosaicking and subletting procedures were executed on the three images. The moderate resolution images of landsat-8 (30 m spatial resolution) and ASTER (15 m) had been fused by the relatively high spatial resolution of Sentinel-2A (10 m). This process is performed by using a pan-sharpening technique and offering a suitable scale to detect bostonite dyes. Finally, image processing algorithms including False Color Combination (FCC), Decorrelation Stretch (DS), band ratios (BR), Principal Component Analysis (PCA), and Minimum Noise Fraction (MNF) have been employed to create lithologic, structural and radioactive minerals maps.

Although FCC is traditional and straightforward, it can be helpful in exploring the geological contacts. The DS method is considered an effective technique in detecting geological contact through reducing the cross-correlation between the spectral bands. It is characterized by its efficiency in detecting the rock units and alteration zones. The minerals' abundance can be detected by using band ratio techniques [16]. The PCA algorithm is able to convert the spectral bands into fewer independent bands.

3.2. Radioactive Detection

To determine radionuclide concentrations, gamma-ray spectrometry was performed. Prior to analysis, fifteen sediment samples (400 g each) from the Um Dwiela region were sealed and stored for a minimum of 21 days to establish secular radioactive equilibrium. Spectrometric analysis was conducted at the Nuclear Material Authority employing a Bicron NaI(Tl) analyzer with a 76 × 76 mm scintillation crystal. The concentrations of ^{40}K, ^{232}Th, and ^{238}U were derived from the 1460.8 keV (^{40}K), 238.6 keV (^{212}Pb for ^{232}Th), and 1764.5 keV (^{214}Bi for ^{238}U) gamma peaks, respectively. Comprehensive methodology regarding energy calibration, uncertainties, and detection limits are documented in the Supplementary Materials.

3.3. Mineralization

Heavy mineral separation was carried out on representative samples using bromoform as a heavy liquid. The separated fractions were subsequently processed through a Frantz isodynamic magnetic separator to partition minerals according to their magnetic susceptibility. Identification of the extracted mineral phases was performed at the Nuclear Materials Authority laboratories using an Environmental Scanning Electron Microscope (ESEM, Phillips XL-30, Philips, Amsterdam, The Netherlands), with complementary verification conducted under a binocular microscope (Supplementary Materials).

4. Results

4.1. Lithological and Mineralogical Mapping

4.1.1. Lithological Discrimination

In the study area, the bostonite dykes intruded into the volcanogenic metasediments and metavolcanics (Figure 2). Therefore, the country rocks and their dykes were paid attention in the mapping process. As mentioned above, we adopted a number of image processing methods such as FCC, DS, BR, and PCA to map the country rocks and bostonite dykes. The different spectral contrasts of the different rock types of outcrops can be

shown in unlike textural colors. The FCC image of RGB-11 8 2 of Sentinel-2 (Figure 4a) discriminated the different rock types in the study area and enhanced the ribbon like of NE bostonite dyke. Volcanogenic metasediments appear as moderate brown colors, whereas the metavolcanics exhibited dark brown color.

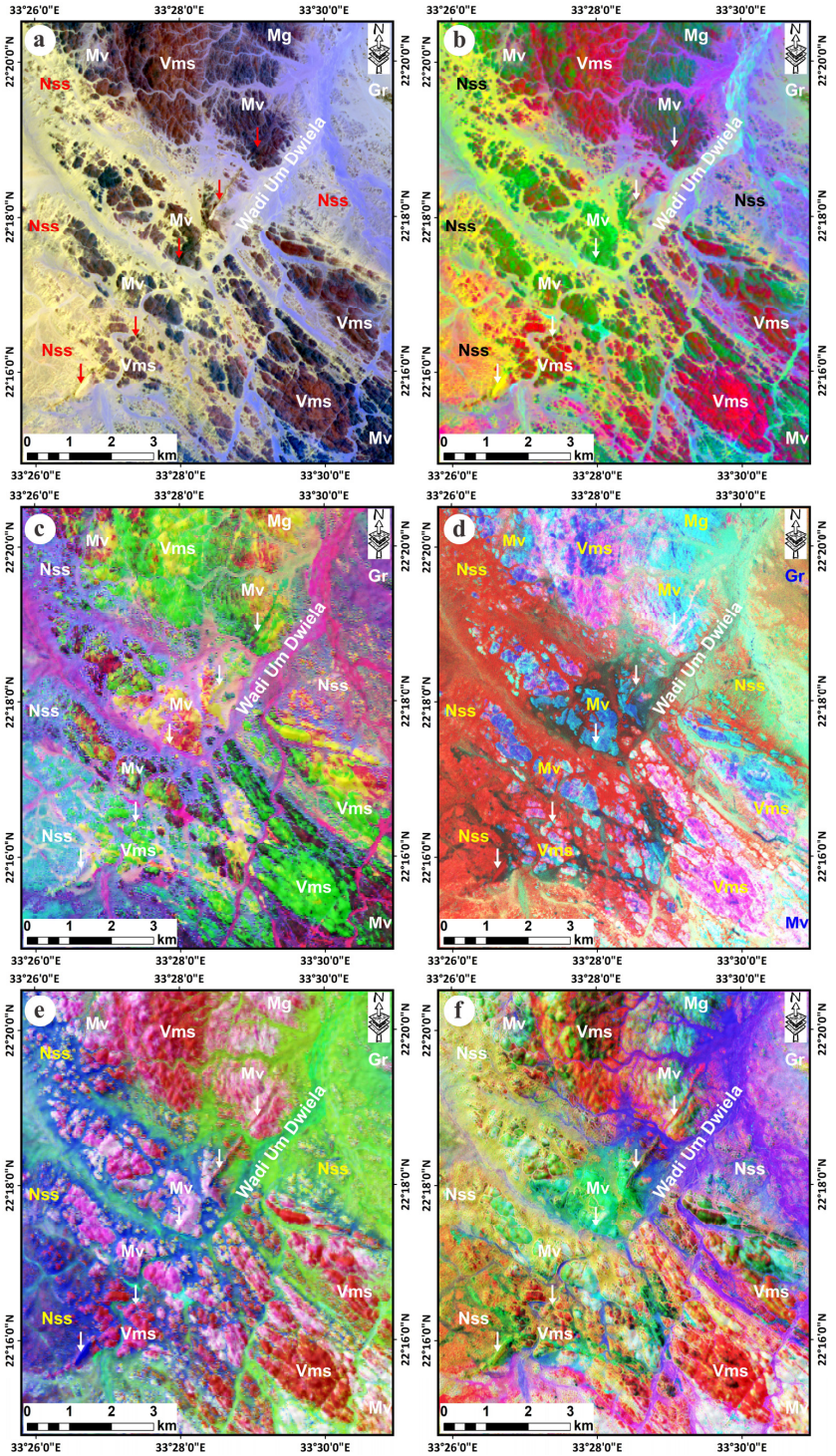

Note: Mvs: volcanogenic metasediments, Mv: intermediate to basic metavolcanics, Mg: metagabbros, Gr: microgranite, Nss: Nubian sandstone.

Figure 4. The lithological discrimination of: (**a**) FCC band composite of 11 8 2 in RGB of Sentinel-2, (**b**) decoration stretched of bands 7 5 3 of Landsat-8, (**c**) band ratio of 6/7, 6/5, 4/2 in RGB of Landsat-8, (**d**) band ratio of 12/11. 4/8, 3/4 in RGB of Sentinel-2, (**e**) PCA-123 in RGB of Landsat-8, and (**f**) PCA-432 in RGB of Sentinel-2.

The specific bands of 7, 5, 3 of Landsat-8 are subjected to the decorrelation stretching technique (DS) and produce a fantastic colorful image in Figure 4b. This decorrelated image is effectively differentiated between the two main country rocks of the bostonite dykes into bright shades of color. Volcanogenic metasediments are successfully classified as bright bloody red color, whereas intermediate to basic metavolcanics are enhanced by olive to dark green colors due to their different mineralogical contents (Figure 4b). The NE bostonite dyke can be easily detected visually by its high relief, ribbon-like, purple color in the groundmass of the green color of the metavolcanics. Band ratio (BR) algorithm is one of the most effective image processing techniques, especially in the arid regions [17]. The present work performed two band ratios of 6/7, 6/5, 4/2 in RGB of Landsat-8 and 12/11. 4/8, 3/4 in RGB of Sentenial-2 (Figure 4c,d). The two selected band ratios magnificently delineated the two country rock types of volcanogenic metasediments and metavolcanics and bostonite dyke. In the band ratio of 6/7, 6/5, 4/2 in RGB of Landsat-8, volcanogenic metasediments were represented by a bright green color, whereas metavolcanics were distinguished by shades of red and yellow colors (Figure 4c). The volcanogenic metasediments are illustrated as a whitish purple color in the band ratio of 12/11, 4/8, 3/4 in RGB of Sentenial-2 (Figure 4d), whereas the metavolcanics exhibited a cynic blue color. The distinct green/yellow and magenta colors of bostonite dyke can be detected obviously in the two images (Figure 4c,d). The high contrast colors of the rock units in Figure 4c show the offset of the NW strike slip faults in the country rocks and dykes, whereas unsensed faults and jointing appear in Figure 4d.

Moreover, principal component composites are adopted in the present study as one of the most informative image processing techniques. The PCA of PCA-321 of Landsat-8 and PCA-432 of Sentinel-2 (Figure 4e,f) are generated. The two images fantastically differentiated the two country rock units, even small masses and the NE bostonite dyke. The red color characterizes the volcanogenic metasediments where the whitish violet represents the metavolcanics in Figure 4e. Also, the volcanogenic metasediments exhibit yellowish red pixels and metavolcanics were enhanced as cynic pixels in Figure 4f. The positive-relief bostonite dyke can be easily noticed in the two images with distinct colors and linear shapes in the two images. The strike slip fault offset and jointing can be detected dramatically in the two images due to the tonal variation. These are classified image processing techniques that produced a fantastic detailed geologic map of the study area (Figure 2). This map is presented here as a newly geologic map of the Um Dwiela area, which is verified by fieldwork, rock samples, and petrography.

4.1.2. Hydrothermal Alterations and Related Radioactive Mineral Detection

Bostonite dykes are felsic to intermediate alkaline dykes that are commonly enriched in radioactive minerals. These dykes are rich in potassium feldspar and commonly associated with hydrothermal alteration and mineralization. Therefore, the successful detection using remote sensing data depends on the delineation of alteration minerals associated with dykes and spectral signature of feldspar rich rocks. Fortunately, the bostonite contents of K-feldspar, sericite, kaolinite, and iron oxides have diagnostic absorption in the SWIR region, where K-feldspar has a distinctive absorption in wavelengths of 1.25, 1.48, 2.20 μm, sericite in 2.20 μm, kaolinite in 2.16–2.21 μm, and iron oxides in 0.52–0.95 μm.

Consequently, the identifying hydrothermal alterations zones and their radioactive mineralization can be discovered successfully by the detection of alteration minerals such as kaolinite, chlorite, hematite, illite, and sericite [18,19]. The present study adopted hydrothermal alteration mineral indices of ASTER data, which was proposed by Cudahy and Hewson [20]. Figure 5a represents the band ratio of band 11/band 12 of Sentinel-2 which highlighted the rich pixels of clay minerals. The bight pixels reflect the most probable

areas rich with alteration minerals where the NE bostonite dyke can obviously detected as linear bright pixels in the grey background of the country rocks. We performed here three spectral mineral indices of the six of Ninomiya [21] to detect the alteration zones and related radioactive mineralization. The OH-bearing mineral index ((7/6) × (4/6)), kaolinite index, KLI ((4/5) × (8/6)), and alunite index, ALI ((7/5) × (7/8)) are show in Figures 5b, 5c and 5d, respectively.

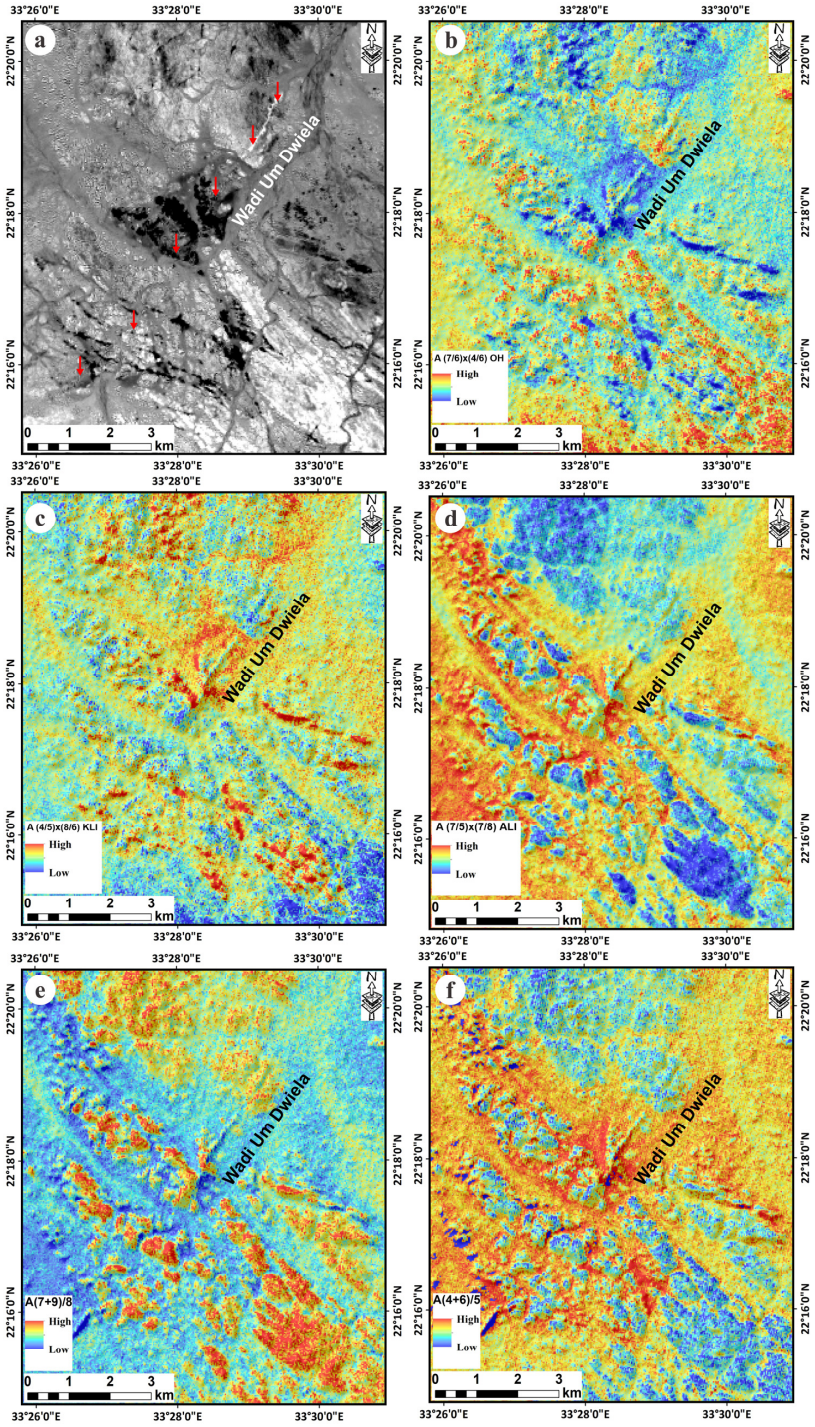

Note: The present study used pseudo color for the grey scale image indices for clarification.

Figure 5. (**a**) The band ratio of 11/12 of Sentinel-2, ASTER mineral indices: (**b**) OH-bearing minerals index, OHI, (**c**) Kaolinite index, KLI, (**d**) Alunite index, ALI, (**e**) chlorite/epidote index, and (**f**) sericite/kaolinite index.

The produced images mostly presented in grey scale and the bright pixels highly reflect the abundance and spatial distribution of the alteration minerals, where the images are produced here by pseudo color to improve the high concentration of the target altered mineral(s) by red color, which can be detected obviously. It is noticed that the OH-bearing minerals, kaolinite and alunite offer high concentration around and over the NE bostonite dyke (Figure 5b–d). It seems that the bostonite dyke have a high concentration of the alteration minerals which in turn produce a high concentration of radioactive mineralization. Two spectral alteration minerals proposed by Cudahy and Hewson [20] are applied here, which are the chlorite/epidote index (7 + 9)/8 and sericite/kaolinite index (4 + 6)/5 (Figures 5e and 5f, respectively). Moreover, regarding the high concentration of the alteration minerals in (Figure 5b–d), there is also a high concentration of sericite, chlorite and epidote around and over the NE bostonite dyke (Figure 5e,f). The high relief of the bostonite dyke make the detection of the concentration of these minerals easy. Finally, the high percentage of these minerals are an important indicator of the high potential concentration of radioactive minerals which are also verified by chemical analysis.

4.2. Distribution and Concentration of Radioelements

The activity concentrations of ^{40}K, ^{238}U, and ^{232}Th were determined in 15 rock samples from the Um Dwiela area using NaI(Tl) gamma-ray spectrometry (Table 1). They ranged from 751.2 to 1533.70 Bq/kg for ^{40}K, 12.4 to 1636.8 Bq/kg for ^{238}U, and 24.24 to 1272.6 Bq/kg for ^{232}Th (Figure 6a). These values exhibit considerable variability and are notably elevated compared to established global averages [1,22].

Table 1. Radionuclide activities and ratios in the Um Dwiela samples.

Sa. No	^{40}K Bq/kg	^{238}U Bq/kg	^{232}Th Bq/kg	^{238}U/^{232}Th	^{238}U/^{40}K	^{232}Th/^{40}K	Total Activity Bq/kg
Ud1	1533.70	1636.80	1272.60	1.15	0.96	0.83	4271.50
Ud2	1439.80	1351.60	759.52	1.59	0.84	0.53	3409.22
Ud3	1471.10	1388.80	775.68	1.60	0.85	0.53	3489.98
Ud4	1502.40	1314.40	1119.08	1.05	0.78	0.74	3798.08
Ud5	1001.60	136.40	165.64	0.74	0.12	0.17	1289.34
Ud6	876.40	49.60	60.60	0.73	0.05	0.07	981.40
Ud7	907.70	111.60	76.76	1.30	0.11	0.08	1084.36
Ud8	1502.40	483.60	513.08	0.84	0.29	0.34	2448.38
Ud9	1064.20	558.00	395.92	1.26	0.47	0.37	1959.62
Ud10	1220.70	1091.20	614.08	1.59	0.80	0.50	2811.58
Ud11	1314.60	892.80	735.28	1.09	0.61	0.56	2849.08
Ud12	907.70	37.20	40.40	0.82	0.04	0.04	981.40
Ud13	845.10	24.80	32.32	0.69	0.03	0.04	899.62
Ud14	782.50	37.20	48.48	0.69	0.04	0.06	864.28
Ud15	751.20	12.40	24.24	0.46	0.01	0.03	786.54
Min	751.20	12.40	24.24	0.46	0.01	0.03	786.54
Max	1533.70	1636.80	1272.60	1.60	0.96	0.83	4271.50
Av.	1141.41	608.43	442.25	1.04	0.40	0.33	2128.29
Sd	285.47	587.63	408.01	0.36	0.36	0.27	1192.36

The enrichment of U in the analyzed samples typically occurs as U^{4+} within accessory minerals (e.g., zircon). Hydrothermal fluids interact with the host rocks under oxidizing conditions, converting insoluble U^{4+} to soluble U^{6+} (as uranyl ions). The uranyl complexes migrate through fracture networks. Upon encountering reducing conditions, U^{6+} precipitates as secondary minerals such as kasolite and uranothorite. The NE-SW structural trends observed in the Um Dwiela area (confirmed by field mapping) served as preferential fluid

pathways, explaining the localized high-grade U enrichment at dyke contacts and within altered zones.

The total activity per sample ranged from 786.54 to 4271.5 Bq/kg, with a mean value of 2128.29 ± 1192.36 Bq/kg, substantially exceeding the internationally recognized safety limit of 420 Bq/kg [23–25]. The wide range in activity concentrations reflects heterogeneous radionuclide distribution across the study area. This spatial variability, coupled with the elevated radioactive buildup within the dykes, is attributed to a combination of geochemical and hydrothermal processes [1]. The Shapiro–Wilk test (W) (Figure 6b) is used to assess whether a dataset follows a normal distribution [26]. The statistical W and corresponding *p*-values were used as the main parameters for statistical interpretation. For our dataset (n = 15), the test evaluates the null hypothesis that the radionuclide activity concentrations follow a normal distribution. Values of W that are close to 1 (with $p > 0.05$) indicate normality. Our calculated values were: ^{40}K (W = 0.892, $p = 0.068$), ^{238}U (W = 0.684, $p = 0.003$), and ^{232}Th (W = 0.712, $p = 0.005$).

These confirm that ^{238}U and ^{232}Th deviate significantly from normal distribution, while ^{40}K approximates normality ($p = 0.068$, just above the significance threshold). The outcomes of this analysis are presented in the probability map (Figure 6c).

The activity concentrations in the Um Dwiela samples consistently followed the order, ^{40}K > ^{238}U > ^{232}Th. The elevated ^{40}K levels are likely attributable to the leaching of feldspars derived from host rocks, particularly those of granitic origin, with the SiO_2 content of the samples further contributing to K availability [1,27–30]. The relatively high concentrations of ^{238}U and ^{232}Th are probably associated with the presence of accessory radioactive minerals, such as kasolite, uranothorite, xenotime, and monazite.

Radionuclide activity ratios for the Um Dwiela samples exhibit notable deviations from global averages (Table 1). The mean ^{232}Th/^{40}K ratio (0.33) and mean ^{238}U/^{40}K ratio (0.45) are substantially higher than the global average of 0.07 [28,31], reflecting the pronounced enrichment of potassium in the study area. Conversely, the mean ^{238}U/^{232}Th ratio (1.16) exceeds the global average of 1.0, indicating a relative enrichment of U over Th in these rock samples.

The measured activity concentrations (Table 2) are significantly elevated and deviate substantially from both the global average [7] and values reported for comparable geological environments. In Egypt, they exceed those documented for sediments in El Maghrabya, Hankorab, Abu Brush, and Abu Ghusun [2,6], yet remain comparable to those reported for the Um Domi granites [31].

On an international scale, the activities from Um Dwiela are notably higher than those recorded at numerous global sites, including Ijebu, Odeda, and Ondo in Nigeria [1] Karaman, Kastamonu, and Isparta in Turkey; granitic terrains in Italy and the European Union [32]; Asa granites in Nigeria [33]; soils in Spain [34]; and soils in Jeddah, Saudi Arabia [35].

The Um Dwiela bostonite dykes share several characteristics with uranium-bearing alkaline dyke systems as those in Ilímaussaq complex, Greenland. They are peralkaline nepheline syenites with hydrothermal U-enrichment (1000–5000 Bq/kg) associated with monazite minerals [36].

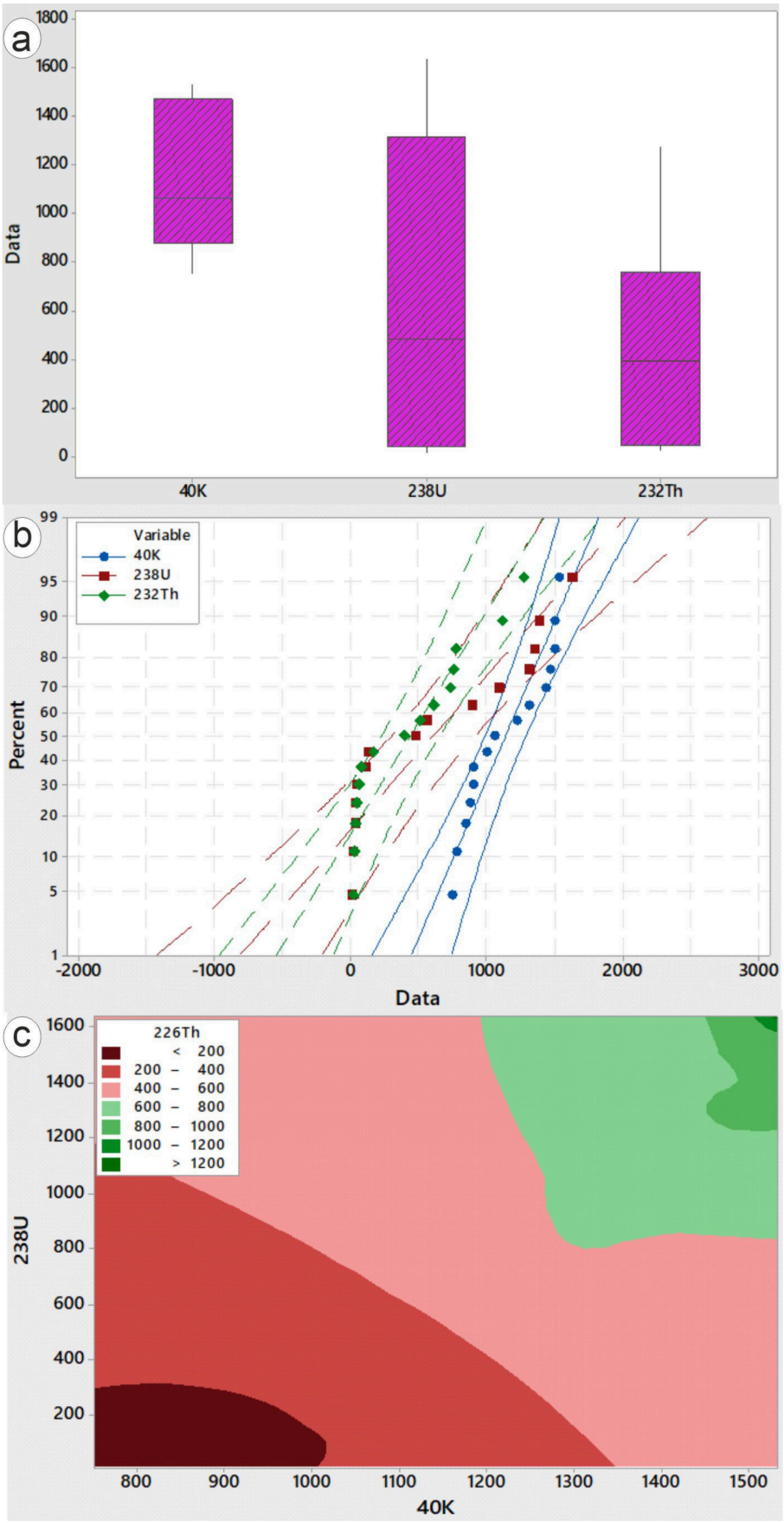

Figure 6. (**a**) Box plot ^{40}K, ^{238}U, and ^{232}Th; (**b**) distribution probability plots for normality testing; and (**c**) contour map of total radioactivity.

Table 2. Comparison of radionuclides from Um Dwiela with those reported in other studies.

	Region	^{238}U (Bq/kg)	^{232}Th (Bq/kg)	^{40}K (Bq/kg)	References
Worldwide	Ijebu, Nigeria	48.21	29.83	2647.88	[1]
	Karaman, Turkey	48.00 ± 2.40	39.18 ± 1.96	143.97 ± 7.20	[37]
	Odeda, Nigeria	55.42	150.10	2056.44	[1]
	Granite block, Italy	110 ± 7	106 ± 9	1330 ± 160	[32]
	EU, Granit Rosa Por	280 ± 40	81 ±14	1060 ± 80	[32]
	Ondo, Nigeria	24.13	20.11	46.48	[1]
	Asa, Nigeria Granite	11.51	15.42	441.06	[33]
	Spain	84	42	1138	[34]
	---	33	45	400	[7]
	Kastamonu, Turkey	48.62 ± 2.43	42.18 ± 2.11	376.39 ± 18.82	[37]
	Bursa, Turkey	36.23 ± 1.81	25.05 ± 1.25	253.85 ± 12.69	[37]
	Isparta, Turkey	22.77 ± 1.14	35.67 ± 1.78	183.55 ± 9.18	[37]
	Jeddah soil	13.14	5.05	139.09	[35]
Egypt	Um Domi granites, Egypt	3797.50	360.57	1197.23	[31]
	Abu Ghusun, Egypt	25.43	29.55	337.06	[38]
	Hankorab coast, Egypt	20.27	23.01	206.27	[39]
	Abu Brush, Egypt	83.70	54.54	1072.03	[2]
	El Maghrabya, Egypt	21.70	20.20	305.18	[6]
	This work	608.43	442.25	1141.41	

5. Discussion

5.1. Radioactive Mineral-Bearing Bostonite

The processed images of Landsat-8, Sentianl-2A and ASTER were efficient in generating lithological, mineralogical and structural maps of the study area. The decorrelated stretching of bands of 753 of Landsat-8 (Figure 4b) and the band ratios, as well as the PCA of Landsat-8 and Sentinel-2, differentiated the country rocks and bostonite dyke dramatically (Figure 4c–f). The newly produced geologic map shows great differences with the pervious geologic map of Saleh [15] and outlines the bostonite dykes in the study area. Moreover, the ASTER mineralogical indices clearly detected the geospatial abundance of the alteration minerals which is necessary for locating the radioactive minerals. The produced images of the five applied indices are presented in Figure 5b–f. They showed that the high abundance of the alteration zones is confined with volcanogenic metasediments, metavolcanics and bostonite dykes. A false color composite image of (OHI, KLI, ALI) indices was generated by combining the three grey scale images into the RGB channels (Figure 7a). The resulting image showed the high distribution of kaolinite and clay minerals are confined to the center of the area around the bostonite dyke. This means that radioactive mineralization is controlled by lithology and alteration such as chlorite, kaolinite, illite, alunite, epidote, and sericite.

Structurally, the study area is dissected by some major strike slip faults oriented in the NW direction and minor faults and fractures trending mostly in NE-SW and NW-SE (Figure 7b,c). The tonal variation of the band ratio of 6/7, 6/5, 6/3 in RGB of Landsat-8 (Figure 7b) successfully enhanced the offset movement of the strike slip faults on the rock units and the NE bostonite dyke. Importantly, it is known that the faults and/or fractures in the area play as pathways for the radioactive bearing solution and in turn mineralization. The previous studies confirmed that radioactive patterns and their high radiometric anomalies in the Eastern Desert of Egypt are controlled by the NE-SW and NW–SE fractures trends [40].

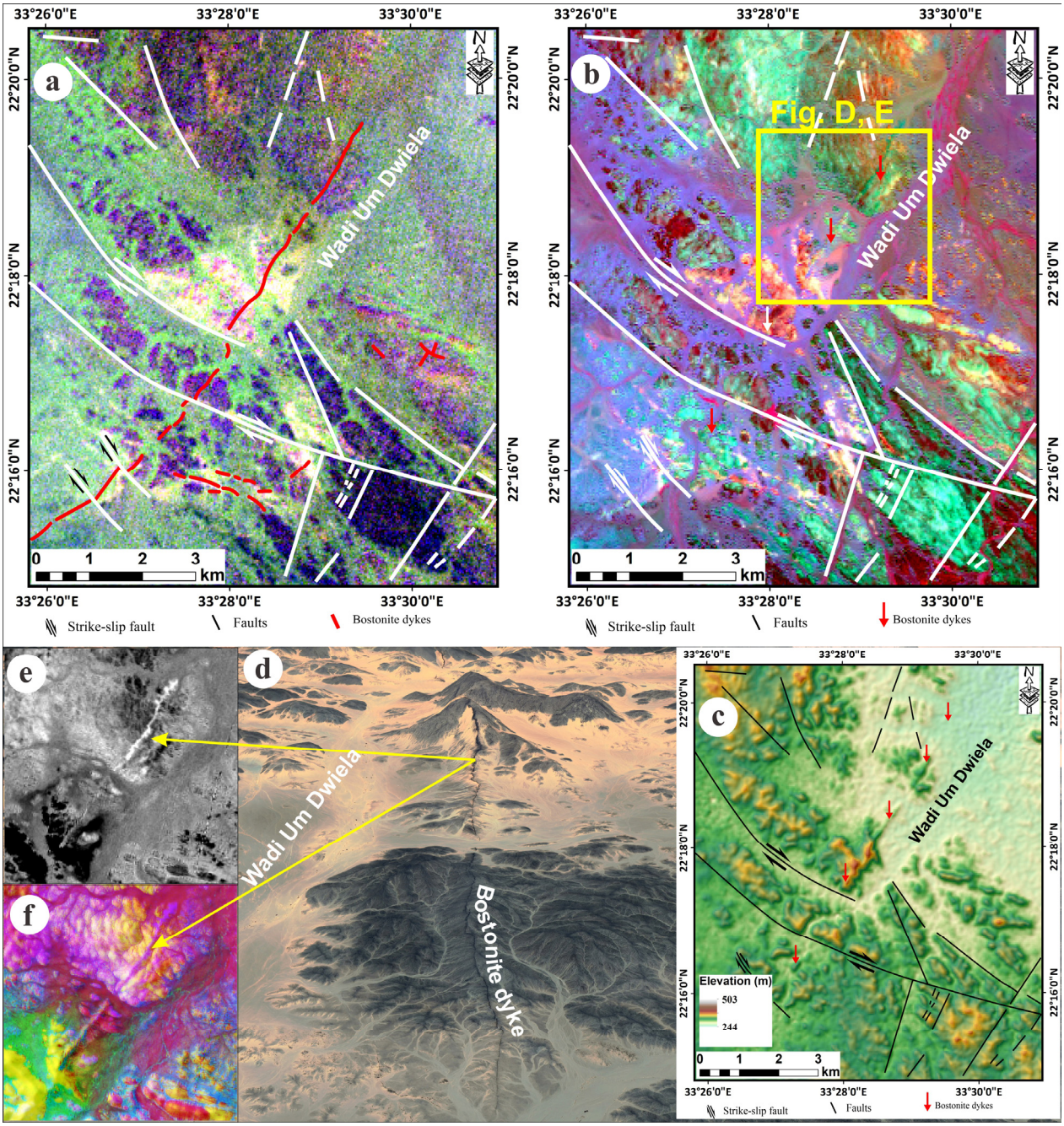

Figure 7. (**a**) FCC ratio images (OHI, KLI, ALI in RGB), (**b**) band ratio of 6/7, 6/5, 6/3 in RGB of Landsat-8 enhance the structural elements, (**c**) digital elevation model (DEM) of SRTM-30 spatial resolution showing the topographical expression of bostonite dyke, (**d**) Google Earth image showing the sharp ridge and linear shape of the bostonite dyke, (**e**,**f**) band ratio of 6/7 of Landsat-8 and PCA-123 of Sentinel-2 showing the spectral contrast of the bostonite dyke relative to the contour rocks.

In addition, the morphological characteristics of the bostonite dyke helped in its detection in the satellite images, where its sharp ridge with high slope angles, ribbon-like, and irregular linearity (Figure 7c,d) are observed. The high-contrast spectral signature of the bostonite dyke also play vital role in its detection from the processed images (Figure 7e,f).

5.2. Indices of Radiation Risk

The measured activity concentrations of ^{232}Th (L_{Th}), ^{238}U (L_U), and ^{40}K (L_K) were used as input data for the calculation of a comprehensive suite of radiological hazard parameters. Following established protocols, the following indices were derived (Table 3): indoor and

outdoor absorbed dose rates (D_{in} and D_{out}); radium equivalent activity (Ra_{eq}); external (H_{ext}) and internal (H_{int}) hazard indices; alpha ($I\alpha$) and gamma ($I\gamma$) representative indices; annual effective doses for indoor (AED_{in}) and outdoor (AED_{out}) exposure; annual gonadal dose equivalent (AGDE); exposure rate (ER); activity utilization index (AUI); and excess lifetime cancer risk for both indoor and outdoor exposure ($ELCR_{in/out}$) (Figure 8).

Table 3. The health risk indices for the Um Dwiela samples.

Sa. No	AUI	I_α	ER	I_γ	Ra_{eq}	AGDE (μSv/y)	D_{rout} (nGy/h)	D_{rin} (nGy/h)	H_{in}	H_{ex}	AED_{out} (mSv/y)	AED_{in} (mSv/y)	$ELCR_{in}$	$ELCR_{out}$
Ud1	186.55	8.18	6973.18	12.33	3574.71	10.86	1615.79	3031.48	14.08	9.66	1.98	14.87	52.05	6.94
Ud2	152.72	6.76	4967.61	8.78	2548.58	7.80	1147.50	2197.01	10.54	6.88	1.41	10.78	37.72	4.93
Ud3	156.36	6.94	5089.46	9.00	2611.30	8.00	1175.57	2251.57	10.81	7.05	1.44	11.05	38.66	5.05
Ud4	166.01	6.57	5922.10	10.48	3030.37	9.21	1373.60	2563.43	11.74	8.19	1.68	12.58	44.01	5.90
Ud5	59.43	0.68	905.55	1.62	450.39	1.43	211.04	389.82	1.59	1.22	0.26	1.91	6.69	0.91
Ud6	46.19	0.25	422.01	0.76	203.74	0.68	98.50	184.16	0.68	0.55	0.12	0.90	3.16	0.42
Ud7	50.91	0.56	590.98	1.06	291.26	0.95	137.23	261.54	1.09	0.79	0.17	1.28	4.49	0.59
Ud8	109.98	2.42	2634.66	4.68	1332.99	4.11	612.76	1132.50	4.91	3.60	0.75	5.56	19.44	2.63
Ud9	88.31	2.79	2367.19	4.19	1206.11	3.71	548.32	1036.14	4.77	3.26	0.67	5.08	17.79	2.35
Ud10	126.12	5.46	4023.49	7.11	2063.33	6.32	929.46	1779.49	8.52	5.57	1.14	8.73	30.55	3.99
Ud11	126.05	4.46	4005.12	7.09	2045.47	6.25	928.81	1737.98	7.94	5.53	1.14	8.53	29.84	3.99
Ud12	46.48	0.19	347.09	0.63	164.86	0.57	81.03	153.10	0.55	0.45	0.10	0.75	2.63	0.35
Ud13	42.68	0.12	289.54	0.53	136.09	0.48	67.68	127.67	0.43	0.37	0.08	0.63	2.19	0.29
Ud14	40.75	0.19	347.46	0.63	166.78	0.56	81.15	151.72	0.55	0.45	0.10	0.74	2.60	0.35
Ud15	37.37	0.06	226.38	0.41	104.91	0.38	53.03	99.67	0.32	0.28	0.07	0.49	1.71	0.23
Min	37.37	0.06	226.38	0.41	104.91	0.38	53.03	99.67	0.32	0.28	0.07	0.49	1.71	0.23
Max	186.55	8.18	6973.18	12.33	3574.71	10.86	1615.79	3031.48	14.08	9.66	1.98	14.87	52.05	6.94
Av.	95.73	3.04	2607.45	4.62	1328.73	4.09	604.10	1139.82	5.23	3.59	0.74	5.59	19.57	2.59
Sd	51.42	2.94	2291.90	4.05	1179.82	3.57	530.32	1001.33	4.76	3.19	0.65	4.91	17.19	2.28

The absorbed dose rates for gamma radiation under outdoor (D_{rout}) and indoor (D_{rin}) conditions were calculated assuming a uniform distribution of naturally occurring radionuclides and a reference height of 1 m above ground level. The computations followed the dosimetric equations established by UNSCAR [7]:

$$D_{rout}\ (nGy/h) = 0.43\ L_U + 0.666\ L_{Th} + 0.042\ L_K \quad (1)$$

$$D_{rin}\ (nGy/h) = 0.92\ L_U + 1.1\ L_{Th} + 0.082\ L_K \quad (2)$$

The radiological hazard parameters calculated for the Um Dwiela samples are presented in Table 3. The D_{rout} ranged from 53.03 to 1615.79 nGy/h, with a mean value of 604 ± 530.32 nGy/h. This mean substantially exceeds the global average of 59 nGy/h [1,8,33,37], indicating a significant potential radiological impact. The D_{rin} exhibited a mean of 1139.82 ± 1001.33 nGy/h, which is notably higher than both the corresponding outdoor rate and the global indoor average of 84 nGy/h (Figure 8a). The large standard deviations associated with both dose rates reflect considerable heterogeneity in radionuclide activity concentrations across the study area. This variability points to a non-uniform geographical distribution of radioelements and suggests localized enrichment of radioactive minerals within specific samples. The elevated radiation levels raise concerns regarding prolonged occupational exposure, particularly for quarry workers. Chronic exposure to such high-dose-rate environments may lead to adverse long-term health effects, including potential damage to tissues and organs [2,9,10].

Following the methodology of [7], the radium equivalent activity (Ra_{eq}) was computed as follows:

$$Ra_{eq}\ (Bq/kg) = L_U + 1.43\ L_{Th} + 0.077\ L_K \quad (3)$$

The calculated Ra_{eq}, which integrates external and internal dose contributions, showed a mean of 1328.73 ± 1179.82 Bq/kg (range: 104.91–3574.71 Bq/kg). This result is not also in tandem with the permissible limit of 370 Bq/kg, collectively affirming the high radiological hazard of the samples [7,9,41].

The calculated radium equivalent activity (Ra_{eq}), which accounts for both external and internal radiation exposures, ranged from 104.91 to 3574.71 Bq/kg, with a mean value of 1328.73 ± 1179.82 Bq/kg. This mean substantially exceeds the internationally accepted safety limit of 370 Bq/kg [41–43], further confirming the significant radiological hazard posed by the Um Dwiela samples.

The external (H_{ex}) and internal (H_{in}) hazard indices serve as essential parameters for evaluating the radiological safety of materials. These indices are also instrumental in regulating indoor exposure to ^{222}Rn and its short-lived decay products. Both indices were calculated following the equations recommended by [7,9]:

$$H_{ex=}\ L_U/370 + L_{Th}/259 + L_K/4810 \quad (4)$$

$$H_{in=}\ L_U/185 + L_{Th}/259 + L_K/4810 \quad (5)$$

For any material to be considered radiologically safe, the external (H_{ex}) and internal (H_{in}) hazard indices must be less than unity [9,44]. To evaluate the potential impact on human health, these indices were calculated for the Um Dwiela samples. The results yielded mean values of 5.23 (range: 0.32–14.08) for H_{in} and 3.59 (range: 0.28–9.66) for H_{ex}, both substantially exceeding the permissible limit of 1 (Figure 8b). These elevated values confirm that the studied rocks pose significant radiological health risks [7].

The annual effective dose (AED) was calculated for both outdoor (AED_{out}) and indoor (AED_{in}) exposure scenarios. The D_r (nGy/h) were converted to effective doses using a conversion factor of 0.7 Sv Gy^{-1}, in accordance with standard occupancy assumptions of 0.2 for outdoor and 0.8 for indoor environments. The resulting AED values were subsequently employed to evaluate the radiological impact of the measured activity concentrations, as presented below:

$$AED_{in} = D_{rin}\ (nGyh^{-1}) \times 8.76\ h \times 0.8 \times 0.7\ (SvGy^{-1}) \times 10^{-3} \quad (6)$$

$$AED_{out}= D_{rout}(nGyh^{-1}) \times 8.76\ h \times 0.2 \times 0.7\ (SvGy^{-1}) \times 10^{-3} \quad (7)$$

The calculated AED ranged from 0.07 to 1.98 mSv/y for AED_{out} and from 0.49 to 14.87 mSv/y for AED_{in}. Both ranges substantially exceed internationally established safety limits [30,43,45]. Notably, the mean AED_{out} value (0.74 mSv/y) is considerably lower than the mean AED_{in} value (5.59 mSv/y) (Figure 8c), highlighting the predominance of indoor radiation exposure in the overall effective dose.

The annual gonadal dose equivalent (AGDE) quantifies the genetically significant component of the annual gamma radiation exposure received by reproductive organs, including the gonads, active bone marrow, and other cells of genetic relevance [10]. The AGDE was calculated using the following formula:

$$AGDE\ (\mu Sv/y) = (3.09L_U + 4.18L_{Th} + 0.314L_K)/1000 \quad (8)$$

The calculated AGDE values for the Um Dwiela samples ranged from 0.37 to 10.33 μSv/y, with a mean of 3.89 μSv/y, significantly exceeding internationally established safety limits.

In addition, the alpha (I_α) and gamma (I_γ) representative level indices were computed to further assess the radiological hazard. These indices were derived using the equations recommended by [9], as follows:

$$I_\gamma = L_U/200 \quad (9)$$

$$I_\gamma = L_U/300 + L_{Th}/200 + L_K/3000 \quad (10)$$

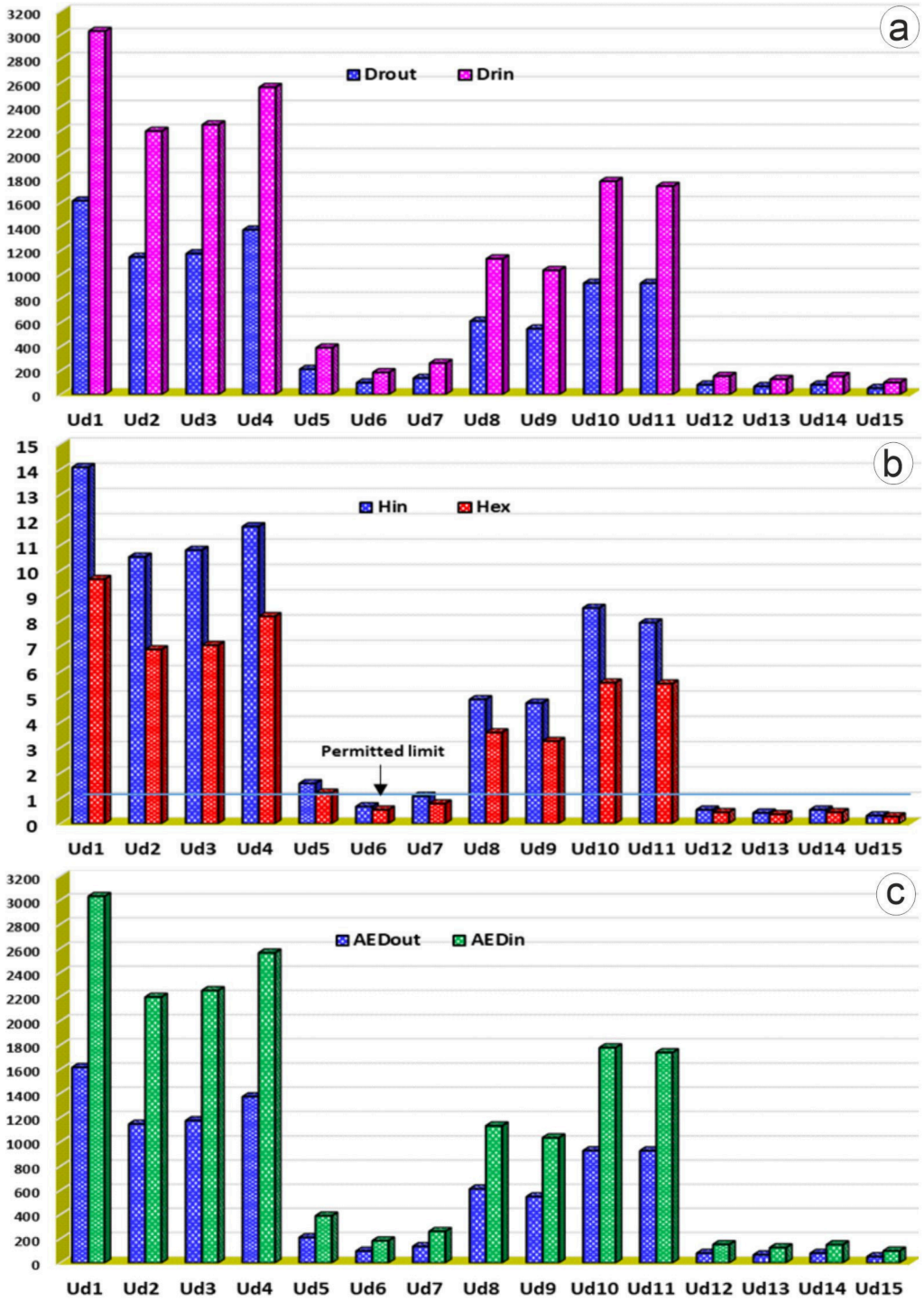

Figure 8. Histograms reveal the relationships between the (**a**) indoor and outdoor absorbed dose rates (Dr_{in} and Dr_{out}); (**b**) external (H_{ex}) and internal (H_{in}) hazard indices; and (**c**) annual effective doses for indoor (AED_{in}) and outdoor (AED_{out}) exposure.

The calculated I_α and I_γ radiation indices yielded mean values of 3.04 ± 2.94 and 4.62 ± 4.05, respectively. Both indices substantially exceed the safety threshold of 1, confirming an elevated radiological hazard potential associated with these radiation types.

The activity utilization index (AUI) estimates the combined radiation dose contribution from naturally occurring radionuclides in rocks. An AUI value below 1 indicates relatively low radiation exposure risk [1]. The AUI was computed using the following formula:

$$AUI = \lfloor L_U/50 \rfloor 0.462 + \lfloor L_{Th}/50 \rfloor 0.604 + \lfloor L_K/500 \rfloor 0.0417 \quad \leq 2 \qquad (11)$$

The calculated AUI values ranged from 37.37 to 186.55, with a mean of 95.73. These results are markedly elevated compared to established international safety limits [46,47], further confirming an elevated radiological hazard posed by the Um Dwiela samples.

The exposure rate (ER) quantifies the gamma radiation dose that individuals may receive from a given source, typically expressed in microrems per hour ($\mu R\ h^{-1}$). This parameter was employed to evaluate the gamma radiation exposure from the Um Dwiela samples following the guidelines of [7], using the formula

$$ER\ (\mu Rh^{-1}) = 1.90L_U + 2.82L_{Th} + 0.179L_K \quad (12)$$

The calculated ER values for the examined samples ranged from 226.38 to 6973.18 μRh^{-1}, with a mean of 2607.45 μRh^{-1}. These values substantially exceed both internationally established safety limits and comparable results reported in other studies, such as those by [1] further confirming the elevated radiological hazard of the area.

Excess lifetime cancer risk (ELCR) estimates an individual's probability of developing cancer over a lifetime as a result of exposure to radionuclides. This parameter is particularly relevant for assessing the long-term health risks to individuals working or residing near quarry sites, where cumulative radionuclide exposure may occur. The ELCR was calculated for both outdoor ($ELCR_{out}$) and indoor ($ELCR_{in}$) exposure scenarios using the following formulas UNSCAR [7]:

$$ELCR_{out} = AED_{out} \times 70\ (y) \times 0.05\ (S/v) \quad (13)$$

$$ELCR_{in} = AED_{in} \times 70\ (y) \times 0.05\ (S/v) \quad (14)$$

The calculated mean ELCR values were 2.59×10^{-3} for outdoor exposure and 19.57×10^{-3} for indoor exposure. Both values substantially exceed the recommended reference levels of 2.9×10^{-4} for outdoor and 1.0×10^{-3} for indoor environments [1,5,48]. These elevated values indicate a significant lifetime carcinogenic risk to the public from the examined samples.

Public health risks: The hazard indices presented here are theoretical calculations based on laboratory measurements of discrete samples. While these results indicate radionuclide concentrations exceeding international safety guidelines, actual health risks to human populations would depend on: (1) duration and frequency of exposure; (2) distance from the source; (3) degree of material disturbance (e.g., quarrying); (4) dust inhalation pathways; and (5) local background dose rates. Field gamma-ray surveys and ambient dose equivalent rate measurements are required to validate these laboratory-based hazard assessments.

5.3. Mineralogy

The exceptionally high concentrations of radionuclides observed in the studied samples can be linked to several interconnected geological processes. Hydrothermal alteration was a key factor, as it mobilized uranium from the original granite matrix and precipitated it in areas with intense fluid–rock interaction, such as fractures, shear zones, and altered domains. Metasomatic processes further contributed to uranium enrichment via chemical exchange between hydrothermal fluids and the host granites, concentrating U in specific mineral phases and altered zones. Additionally, structural features like faults and shear zones facilitated fluid flow and served as conduits for uranium-bearing fluids, ultimately leading to localized but extreme U enrichment within the granitic rocks [35,49].

A mineralogical investigation of the Um Dwiela bostonite has identified the presence of kasolite, uranothorite, xenotime, monazite, and zircon.

These identified radioactive mineral assemblage provides critical insights into the paragenetic evolution of the Um Dwiela dykes. Kasolite, as a secondary uranyl silicate,

confirms post-magmatic supergene alteration under oxidizing conditions. Uranothorite, interpreted as a hydrothermal alteration product of primary thorite, indicates the influx of U- and Th-bearing hydrothermal fluids following dyke emplacement. The presence of xenotime and monazite with significant U substitution demonstrates that the hydrothermal fluids were enriched in REEs [50]. Collectively, this mineral assemblage is characteristic of late-stage fluid saturation and hydrothermal overprinting.

As a secondary product of uraninite oxidation, kasolite exhibits a distinct monoclinic crystal structure. This structure is based on the uranophane sheet anion topology, featuring prominent uranyl silicate layers. The mineral is identifiable by its radial texture and colors ranging from ocher yellow to brownish yellow. ESEM data indicates that its chemical composition consists of 40.0% U, 22.6% Pb, 18.0% K, 16.4% Si, and 3.0% Al (Figure 9a).

The presence of uranothorite, formed by the decomposition of thorite in an oxidizing and acidic hydrothermal environment, confirms that the area was influenced by U- and Th-bearing hydrothermal solutions. As shown in Figure 9b, the mineral's composition is predominantly 46.0 wt% Th, with significant U (23.11 wt%), along with 12.42 wt% Si, 5.43 wt% Y, 3.45 wt% Al, and 2.18 wt% Yb (Figure 9b).

Xenotime, identified as YPO_4, is characterized by its prismatic crystals with distinctive pyramidal terminations. Pyle [50] further demonstrated that U, Ca, and Si can significantly substitute for Y. Quantitative SEM-EDS analysis revealed the detailed composition shown in Figure 9c, with 32.08 wt% Y, 4.69 wt% Yb, 5.69 wt% Er, 9.05 wt% Dy, 28.08 wt% P, 3.59 wt% Al, 7.99 wt% Si, 5.27 wt% Gd and 1.48 wt% Mg.

Monazite, with the general formula (LREE, Th, U) PO_4, exhibits remarkable crystal-chemical flexibility, accommodating over 25 different elements within its lattice [50]. It typically forms rounded crystals that may enclose zircon and is recognized for its stability during weathering [51]. SEM-EDS quantification (Figure 9d) shows it consists of 27.05 wt% Ce, 16.89 wt% Nd, 11.63 wt% La, 3.35 wt% Pr, 2.43 wt% Gd, 2.14 wt% Th, 1.48 wt% U, 10.72 wt% P, and 0.78 wt% Ca.

Zircon is characterized by its remarkable diversity in morphology, color, chemical composition, radioactivity, and provenance. Hoskin [52] noted that the development of pyramidal faces is controlled by the major element chemistry. Furthermore, the water content of the magma influences the duration of zircon crystallization and the development of its prism faces. Quantitative SEM-EDS analysis (Figure 9e) revealed the following composition: 52.0 wt% Zr, 39.0 wt% Si, 2.35 wt% Hf, 2.44 wt% Fe, 2.11 wt% Al, 1.10 wt% Ca, and 1.0 wt% K.

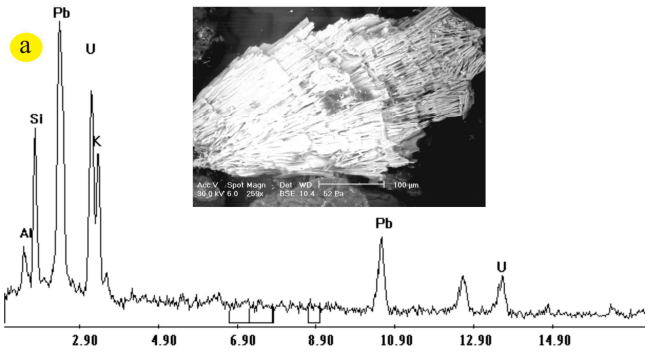

Figure 9. *Cont.*

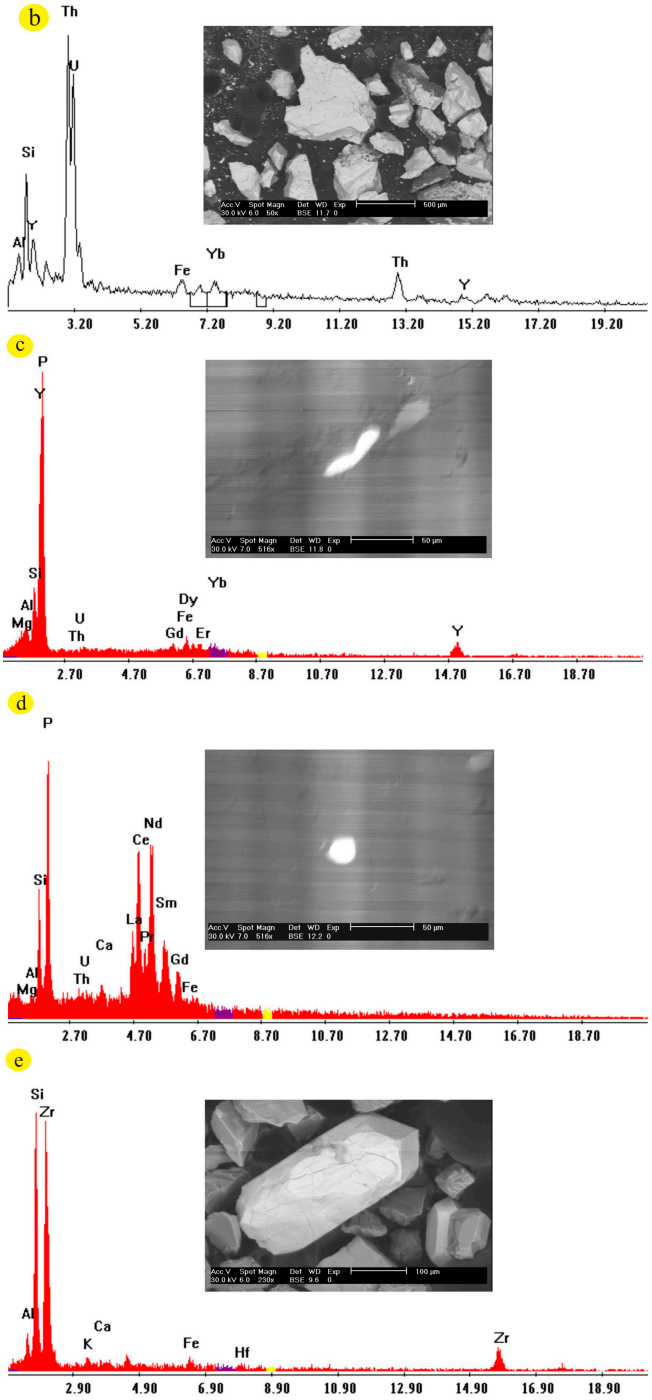

Figure 9. ESEM of the radioactive minerals from the Um Dwiela trachytic dykes: (**a**) kasolite; (**b**) uranothorite; (**c**) xenotime; (**d**) monazite; and (**e**) zircon.

6. Conclusions

A multidisciplinary methodology, incorporating remote sensing, field studies and in-depth mineralogical and radiometric analyses, was applied in this investigation. The integration of the results of multisensor remotely sensed data processing, chemical analysis and fieldwork successfully detect the radioactive probable zones in the study area. The different processing algorithms of remote sensing data effectively enhance the geological contacts, structural elements and locating of the radioactive mineralization zones. The data provided that radioactive mineralization is confined to the bostonite dykes and controlled by lithology and structures. The findings are in strong agreement, demonstrating that the

radiological concern is high. The Um Dwiela bostonite, which strikes NE-SW over approximately 12.0 km with a width of 1–13.0 m, shows evidence of intense hydrothermal alteration. The systematic spatial correlation between alteration intensity (silicification, fluoritization, ferrugination, and kaolinitization) and elevated ^{238}U (608.43 ± 587.63 Bq/kg, mean) and ^{232}Th (442.25 ± 408.01 Bq/kg) activities demonstrates that hydrothermal processes were the dominant enrichment mechanism. This finding has implications for exploration targeting in the southern Egyptian Shield: structurally controlled alteration zones that represent high-priority targets for U-Th-mineralization. Consequently, every derived radiological hazard index indicates an elevated radiological hazard potential that warrants further in situ investigation and, if confirmed, appropriate monitoring protocols. The mineralogical study of the Um Dwiela bostonite revealed the presence of kasolite, uranothorite, xenotime, monazite, and zircon. The assemblage of these radioactive minerals within the dykes underscores the critical influence of hydrothermal processes on their genesis.

Supplementary Materials: The following supporting information can be downloaded at https://www.mdpi.com/article/10.3390/min16060621/s1.

Author Contributions: Conceptualization, E.S.R.L., G.M.S.; Data curation, E.S.R.L.; Funding acquisition, T.A.; Investigation, E.S.R.L., S.Z.K., G.M.S.; Methodology and sample collection, G.M.S.; Software, E.S.R.L.; Supervision, E.S.R.L., B.A.E.-B., T.A., S.Z.K., M.S., I.V.S.; Validation, E.S.R.L., M.S., I.V.S.; Visualization, E.S.R.L., G.M.S., S.Z.K., B.A.E.-B., T.A.; Writing—original draft, E.S.R.L.; Writing—review and editing, E.S.R.L., G.M.S., B.A.E.-B., S.Z.K., T.A., I.V.S. and M.S. All authors have read and agreed to the published version of the manuscript.

Funding: This work was supported and funded by the Deanship of Scientific Research at Imam Mohammad Ibn Saud Islamic University (IMSIU) (grant number IMSIU-DDRSP2602).

Data Availability Statement: The original contributions presented in this study are included in the article/Supplementary Materials. Further inquiries can be directed to the corresponding authors.

Conflicts of Interest: The authors declare no conflicts of interest.

References

1. Jegede, D.O.; Afolabi, T.A.; Agunbiade, F.O.; Afolabi, T.A.; Ogundiran, O.O.; Gbadamosi, M.R.; Sojinu, S.O.; Ojekunle, O.Z.; Varanusupakul, P. Spatial Distribution and Radiological Hazards Assessment of Naturally Occurring Radionuclide Materials in Soil from Quarry Sites in Ogun State, Nigeria. *Environ. Monit. Assess.* **2025**, *197*, 575. [CrossRef]
2. Lasheen, E.S.R.; Semary, H.E.; Kamh, S.Z.; Saleh, G.M. Advanced Remote Sensing Techniques for Mapping Lithological Units and Radioactive Alteration in the Southern Eastern Desert, Egypt: Petrological and Radiological Hazards Determination. *Adv. Space Res.* **2026**, *77*, 5818–5836. [CrossRef]
3. Özden, S.; Pehlivanoğlu, S.A.; Günay, O. Evaluation of Natural Radioactivity in Soils of Konya (Turkey) and Estimation of Radiological Health Hazards. *Environ. Monit. Assess.* **2023**, *195*, 1523. [CrossRef]
4. Saleh, G.M.; El-Badry, B.A.; Sami, M.; Alhazani, T.; Amer, O.T.; Sanislav, I.V.; Lasheen, E.S.R. Mineralization and Radioactive Potential of Magal Gebreel Rocks, South Eastern Desert, Egypt: Health Risk Evaluation. *Nucl. Eng. Technol.* **2026**, *58*, 104165. [CrossRef]
5. Taşköprü, C.; Özden, S.; Günay, O.; Aközcan Pehlivanoğlu, S.; Saç, M.; İçhedef, M. Natural and Artificial Radioactivity Levels and External Radiation Dose Levels of Sand Samples Collected from Lara Beach, Antalya, Türkiye. *J. Radioanal. Nucl. Chem.* **2024**, *333*, 5791–5797. [CrossRef]
6. Lasheen, E.S.R.; El-Badry, B.A.; Mohamed, W.H.; Khouqeer, G.A.; Sanislav, I.V.; Sami, M. Radioactivity and Aeromagnetic of Magmatic Suites, Arabian Nubian Shield: Petrological and Health Risk Characteristics. *J. Radiat. Res. Appl. Sci.* **2025**, *18*, 101910. [CrossRef]
7. UNSCEAR (Ed.) *Sources and Effects of Ionizing Radiation: United Nations Scientific Committee on the Effects of Atomic Radiation: UNSCEAR 2008 Report to the General Assembly, with Scientific Annexes*; United Nations: New York, NY, USA, 2010.
8. Zare, M.R.; Mostajaboddavati, M.; Kamali, M.; Abdi, M.R.; Mortazavi, M.S. 235U, 238U, 232Th, 40K and 137Cs Activity Concentrations in Marine Sediments along the Northern Coast of Oman Sea Using High-Resolution Gamma-Ray Spectrometry. *Mar. Pollut. Bull.* **2012**, *64*, 1956–1961. [CrossRef]

9. Isinkaye, M.O.; OlaOlorun, O.A.; Chandrasekaran, A.; Adekeye, A.S.; Dada, T.E.; Tamilarasi, A.; Sathish, V.; Khandaker, M.U.; Almujally, A.; Tamam, N.; et al. Quantification of Radiological Hazards Associated with Natural Radionuclides in Soil, Granite and Charnockite Rocks at Selected Fields in Ekiti State, Nigeria. *Heliyon* **2023**, *9*, e22451. [CrossRef] [PubMed]
10. Kefalati, M.; Masoudi, S.F.; Abbasi, A. Effect of Human Body Position on Gamma Radiation Dose Rate from Granite Stones. *J. Environ. Health Sci. Eng.* **2021**, *19*, 933–939. [CrossRef] [PubMed]
11. Khaleal, F.M.; Tahoon, M.A.; Saleh, G.M.; Kamar, M.S.; Zakaly, H.M.H.; Zidan, I.H.; Al-Mur, B.A.; Alarif, S.S.; Lasheen, E.S.R. Dolphin-Shaped Island: Exploring the Natural Resources and Radiological Hazards of Wadi El Gemal Island. *Mar. Pollut. Bull.* **2023**, *194*, 115367. [CrossRef]
12. Lasheen, E.S.R.; El-Badry, B.A.; Kamh, S.Z.; Leybourne, M.; Alhazani, T.; Sanislav, I.V.; Sami, M. Integration of Remote Sensing, Geochemistry, and Pb Isotopes to Unravel the Origin of the Wadi Mahasin Felsic Volcanism, Central Eastern Desert, Egypt. *Minerals* **2026**, *16*, 545. [CrossRef]
13. Rashwan, M.A.; Lasheen, E.S.R.; Abdelwahab, W.; Azer, M.K.; Zakaly, H.M.H.; Alarifi, S.S.; Ene, A.; Thabet, I.A. Physico-Mechanical Properties and Shielding Efficiency in Relation to Mineralogical and Geochemical Compositions of Um Had Granitoid, Central Eastern Desert, Egypt. *Front. Earth Sci.* **2023**, *11*, 1228489. [CrossRef]
14. Zoheir, B.; Emam, A.; Abdel-Wahed, M.; Soliman, N. Multispectral and Radar Data for the Setting of Gold Mineralization in the South Eastern Desert, Egypt. *Remote Sens.* **2019**, *11*, 1450. [CrossRef]
15. Saleh, G.M. *Uranium Mineralization in the Granites from Gebel Abu Brush—Gebel Um Krush Area, South Eastern Desert, Egypt*; Report Geology; Egyptian Nuclear Materials Authority: Cairo, Egypt, 2001; p. 45.
16. Sabins, F.F. Remote Sensing for Mineral Exploration. *Ore Geol. Rev.* **1999**, *14*, 157–183. [CrossRef]
17. Abd El-Wahed, M.; Kamh, S.; Abu Anbar, M.; Zoheir, B.; Hamdy, M.; Abdeldayem, A.; Lebda, E.M.; Attia, M. Multisensor Satellite Data and Field Studies for Unravelling the Structural Evolution and Gold Metallogeny of the Gerf Ophiolitic Nappe, Eastern Desert, Egypt. *Remote Sens.* **2023**, *15*, 1974. [CrossRef]
18. Ahmed, S.B.; Elhusseiny, A.A.; Azzazy, A.A.; El-Qassas, R.A.Y. Utilization of Airborne Geophysical Data and Remote Sensing to Identify Radioactive and Hydrothermal Alteration Zones in the East Qena Area, Central Eastern Desert, Egypt. *Acta Geophys.* **2025**, *73*, 5437–5463. [CrossRef]
19. El-Qassas, R.A.Y.; Abu-Donia, A.M.; Omar, A.E.A. Delineation of Hydrothermal Alteration Zones Associated with Mineral Deposits, Using Remote Sensing and Airborne Geophysics Data. A Case Study: El-Bakriya Area, Central Eastern Desert, Egypt. *Acta Geod. Geophys.* **2023**, *58*, 71–107. [CrossRef]
20. Cudahy, T.; Hewson, R. ASTER Geological Case Histories: Porphyry-Skarnepithermal, Iron Oxide Cu-Au and Broken Hill Pb-Zn-Ag. In *Annual General Meeting of the Geological Remote Sensing Group 'ASTER Unveiled'*; Burlington House: London, UK, 2002.
21. Ninomiya, Y. A Stabilized Vegetation Index and Several Mineralogic Indices Defined for ASTER VNIR and SWIR Data. In *Proceedings of the IGARSS 2003. 2003 IEEE International Geoscience and Remote Sensing Symposium*; Proceedings (IEEE Cat. No. 03CH37477); IEEE: Toulouse, France, 2003; Volume 3, pp. 1552–1554.
22. Kumar, N.; Khyalia, B.; Yadav, J.; Singh, B.; Gupta, V.; Singh, P.P.; Singh, H.; Dalal, R. Assessment of Natural Radioactivity in Soil around Khetri Copper Belt of Rajasthan, India. *J. Radioanal. Nucl. Chem.* **2024**, *333*, 3185–3194. [CrossRef]
23. Attallah, M.F.; Hilal, M.A.; Mohamed, Y.T. Preliminary Investigations on Reducing the High Radiation Risk Level of TENORM Scale Waste from Petroleum Industry. *Radiochim. Acta* **2018**, *106*, 793–800. [CrossRef]
24. Margineanu, R.M.; Duliu, O.G.; Blebea-Apostu, A.M.; Gomoiu, C.; Bercea, S. Environmental Dose Rate Distribution along the Romanian Black Sea Shore. *J. Radioanal. Nucl. Chem.* **2013**, *298*, 1191–1196. [CrossRef]
25. O'Brien, K.; Sanna, R. The Distribution of Absorbed Dose-rates in Humans from Exposure to Environmental Gamma Rays. *Health Phys.* **1976**, *30*, 71–78. [CrossRef] [PubMed]
26. Kanmi, A.S.; Ibrahim, U.; Goki, N.G.; Rilwan, U.; Sayyed, M.I.; Maghrbi, Y.; Namq, B.F.; Najam, L.A.; Wais, T.Y. Assessment of Natural Radioactivity and Its Radiological Risks in the Soil of Local Government Areas (Asa, Ilorin East, Ilorin South, Irepodun, Moro, and Oyun) in Kwara State, Nigeria. *Case Stud. Chem. Environ. Eng.* **2025**, *11*, 101040. [CrossRef]
27. Arunima, S.; Lekshmi, R.; Jojo, P.J.; Mayeen Uddin, K. A Study on Leaching of Primordial Radionuclides ^{232}Th and ^{40}K to Water Bodies. *Radiat. Phys. Chem.* **2021**, *188*, 109658. [CrossRef]
28. Qureshi, A.A.; Tariq, S.; Din, K.U.; Manzoor, S.; Calligaris, C.; Waheed, A. Evaluation of Excessive Lifetime Cancer Risk Due to Natural Radioactivity in the Rivers Sediments of Northern Pakistan. *J. Radiat. Res. Appl. Sci.* **2014**, *7*, 438–447. [CrossRef]
29. Runsheng, H.; Yan, Z.; Wenlong, Q.; Tianzhu, D.; Mingzhi, W.; Feng, W. Geology and Geochemistry of Zn-Pb(-Ge-Ag) Deposits in the Sichuan-Yunnan-Guizhou Triangle Area, China: A Review and a New Type. *Front. Earth Sci.* **2023**, *11*, 1136397. [CrossRef]
30. Sivakumar, S.; Chandrasekaran, A.; Senthilkumar, G.; Suresh Gandhi, M.; Ravisankar, R. Determination of Radioactivity Levels and Associated Hazards of Coastal Sediment from South East Coast of Tamil Nadu with Statistical Approach. *Iran. J. Sci. Technol. Trans. Sci.* **2018**, *42*, 601–614. [CrossRef]

31. Lasheen, E.S.R.; El-Badry, B.A.; Kamh, S.Z.; Sami, M.; AbdelAll, N.; Sanislav, I.V.; Hasan, S.S.; Saleh, G.M. Multispectral Remote Sensing and Radiometric Data for Delineating Radioelement-Enriched Zones and Their Health Hazards in Um Domi Area, South Eastern Desert, Egypt. *J. Radiat. Res. Appl. Sci.* **2025**, *18*, 102007. [CrossRef]
32. Kuzmanović, P.; Todorović, N.; Nikolov, J.; Hansman, J.; Vraničar, A.; Knežević, J.; Miljević, B. Assessment of Radiation Risk and Radon Exhalation Rate for Granite Used in the Construction Industry. *J. Radioanal. Nucl. Chem.* **2019**, *321*, 565–577. [CrossRef]
33. Orosun, M.M.; Usikalu, M.R.; Oyewumi, K.J.; Achuka, J.A. Radioactivity Levels and Transfer Factor for Granite Mining Field in Asa, North-Central Nigeria. *Heliyon* **2020**, *6*, e04240. [CrossRef]
34. Guillén, J.; Tejado, J.J.; Baeza, A.; Salas, A.; Muñoz-Muñoz, J.G. Environmental Impact of a Granite Processing Factory as Source of Naturally Occurring Radionuclides. *Appl. Geochem.* **2014**, *47*, 122–129. [CrossRef]
35. Al-Mur, B.A.; Aljahdali, M.H.; Almeelbi, T.; Lasheen, E.S.R. Spatial Radionuclide Distribution, Mineralogy, and Radiological Evaluation of the Jeddah Shoreline Sediments, Red Sea, Saudi Arabia. *Environ. Monit. Assess.* **2025**, *197*, 593. [CrossRef] [PubMed]
36. Marks, M.A.W.; Markl, G. The Ilímaussaq Alkaline Complex, South Greenland. In *Layered Intrusions*; Charlier, B., Namur, O., Latypov, R., Tegner, C., Eds.; Springer Geology; Springer: Dordrecht, The Netherlands, 2015; pp. 649–691.
37. Akkurt, I.; Günoğlu, K. Natural Radioactivity Measurements and Radiation Dose Estimation in Some Sedimentary Rock Samples in Turkey. *Sci. Technol. Nucl. Install.* **2014**, *2014*, 950978. [CrossRef]
38. Abdelaal, A.; Saleh, G.M.; Lasheen, E.S.R.; Sami, M.; Khaleal, F.M.; Sanislav, I.V.; Abdalla, F. Heavy Metals and Radioactivity Assessment of the Coastal Sediments at Abu Ghusun, Southern Red Sea, Egypt. *J. Radiat. Res. Appl. Sci.* **2025**, *18*, 101976. [CrossRef]
39. Saleh, G.M.; Lasheen, E.S.R.; Foi, M.; Abdalla, F.; Abdelaal, A. Assessment of Radioactivity and Heavy Metal Pollution Levels in the Coastal Sediments in the Red Sea Region of Sharm El Luli, Egypt. *Water Air Soil Pollut.* **2025**, *236*, 319. [CrossRef]
40. Sherif, H.M. Geology and Uranium Potentiality of Wadi Seih Area, Southwestern Sinai, Egypt. Ph.D. Thesis, Cairo University, Giza, Egypt, 1997.
41. Büyükuslu, H.; Özdemir, F.B.; Öge, T.Ö.; Gökce, H. Indoor and Tap Water Radon (222Rn) Concentration Measurements at Giresun University Campus Areas. *Appl. Radiat. Isot.* **2018**, *139*, 285–291. [CrossRef]
42. Ebyan, O.; Khamis, H.; Ali, H.; Abed, N. Radioactivity and Geochemistry of Wadi El Reddah Stream Sediments, North Eastern Desert, Egypt. *Arab. J. Nucl. Sci. Appl.* **2019**, *53*, 76–87. [CrossRef]
43. Wais, T.Y.; Ali, F.N.M.; Najam, L.A.; Mansour, H.; Mostafa, M.Y.A. Assessment of Natural Radioactivity and Radiological Hazards of Soil Collected from Rabia Town in Nineveh Governorate (North Iraq). *Phys. Scr.* **2023**, *98*, 065304. [CrossRef]
44. Al-Sewaidan, H.A. Natural Radioactivity Measurements and Dose Rate Assessment of Selected Ceramic and Cement Types Used in Riyadh, Saudi Arabia. *J. King Saud Univ.-Sci.* **2019**, *31*, 987–992. [CrossRef]
45. Lasheen, E.S.R.; Alhazani, T.; Saleh, G.M.; El-Badry, B.A.; Sami, M.; Sanislav, I.V.; Abdelaal, A. Trace Metal Enrichment and Radiological Risk in Coastal Sediments: Implications for Ecological and Human Health Safety. *Toxics* **2026**, *14*, 464. [CrossRef]
46. Senthilkumar, G.; Raghu, Y.; Sivakumar, S.; Chandrasekaran, A.; Prem Anand, D.; Ravisankar, R. Natural Radioactivity Measurement and Evaluation of Radiological Hazards in Some Commercial Flooring Materials Used in Thiruvannamalai, Tamilnadu, India. *J. Radiat. Res. Appl. Sci.* **2014**, *7*, 116–122. [CrossRef]
47. Siemon, B.; Ibs-von Seht, M.; Steuer, A.; Deus, N.; Wiederhold, H. Airborne Electromagnetic, Magnetic, and Radiometric Surveys at the German North Sea Coast Applied to Groundwater and Soil Investigations. *Remote Sens.* **2020**, *12*, 1629. [CrossRef]
48. Mudd, G.M. Radon Releases from Australian Uranium Mining and Milling Projects: Assessing the UNSCEAR Approach. *J. Environ. Radioact.* **2008**, *99*, 288–315. [CrossRef]
49. Pavlidou, S.; Koroneos, A.; Papastefanou, C.; Christofides, G.; Stoulos, S.; Vavelides, M. Natural Radioactivity of Granites Used as Building Materials. *J. Environ. Radioact.* **2006**, *89*, 48–60. [CrossRef]
50. Pyle, J.M. Monazite-Xenotime-Garnet Equilibrium in Metapelites and a New Monazite-Garnet Thermometer. *J. Petrol.* **2001**, *42*, 2083–2107. [CrossRef]
51. El-Kammar, A.M.; El-Hazik, N.; Mahdi, M.; Aly, N. Geochemistry of Accessory Minerals Associated with Radioactive Mineralisation in the Central Eastern Desert, Egypt. *J. Afr. Earth Sci.* **1997**, *25*, 237–252. [CrossRef]
52. Hoskin, P.W.O.; Schaltegger, U. The Composition of Zircon and Igneous and Metamorphic Petrogenesis. *Rev. Miner. Geochem.* **2003**, *53*, 27–62. [CrossRef]

Disclaimer/Publisher's Note: The statements, opinions and data contained in all publications are solely those of the individual author(s) and contributor(s) and not of MDPI and/or the editor(s). MDPI and/or the editor(s) disclaim responsibility for any injury to people or property resulting from any ideas, methods, instructions or products referred to in the content.